Geophysical Journal International

Geophys. J. Int. (2024) **236,** 62–77
Advance Access publication 2023 October 23
GJI Applied and marine geophysics

https://doi.org/10.1093/gji/ggad418

Seismoelectric response of 2-D elastic/poroelastic coupled media: a phenomenological approach

F. Bucher,[1] L. B. Monachesi,[2] G. A. Castromán[1] and F. I. Zyserman[1]

[1]*CONICET, Facultad de Ciencias Astronómicas y Geofísicas, Universidad Nacional de La Plata, La Plata,* 1900*, Argentina.*
E-mail: fbucher@fcaglp.unlp.edu.ar
[2]*CONICET, Instituto de Investigaciones Geológicas y Paleobiológicas, Universidad Nacional de Río Negro, Río Negro, R*8332*, Argentina*

Accepted 2023 October 19. Received 2023 July 31; in original form 2023 March 17

SUMMARY

In this paper, we address the study of the seismoelectric response of an elastic medium in contact with a poroelastic half-space. In particular, we advance in the understanding of the generation mechanism of the interface response (IR) and the evanescent electromagnetic (EM) fields occurring at the contact between both media, by proposing a seismoelectric phenomenological model (SPM). Essentially, the model consists of a sequence of electric dipoles that are activated successively, simulating the seismic-to-EM energy conversion taking place with the arrival of a seismic wave at the interface separating the media. We obtained SPM responses for different scenarios and acquisition configurations and compared them with responses computed using a code based on the finite-elements method, which solves the seismoelectric equations in the compressional *P* and vertical shear *SV* waves coupled with the transverse-magnetic (TM) fields (PSVTM) mode. The SPM successfully represents not only the evanescent wave but also the IR within the elastic medium. In particular, we show that the SPM is able to faithfully reproduce the relative amplitudes of both events and their radiation patterns with a minimum computational cost. In this way, it provides a novel insight in the study of the physical phenomenon behind the seismoelectric conversions.

Key words: Electromagnetic theory; Numerical modelling; Wave propagation.

1 INTRODUCTION

Due to the existence of the so-called electric double layer (EDL) in the grain boundaries of fluid-saturated porous media, an electrokinetic phenomenon takes place when a relative motion between the solid matrix and the pore fluid occurs. A seismic wave propagating through this type of media induces a streaming electric current, which acts as a source of electromagnetic (EM) fields. One of these is the coseismic field, which is spatially supported by the seismic wave and, in turn, travels at a seismic velocity. This field, together with the interface response (IR) generated when the seismic wave arrives at an interface between two media with different electrical and/or mechanical properties, are both the main and most studied seismoelectric conversions (Grobbe *et al.* 2020). They differ in their propagation velocity, since the IR propagates with the EM velocity of the medium. Another difference lies in the spatial support, since the IR propagates through the whole space with a 'dipole-like' behaviour (Garambois & Dietrich 2002; Warden *et al.* 2013). Given that it is triggered by an asymmetry in the charge separation produced by a seismic wave (Butler *et al.* 2018; Grobbe *et al.* 2020), the IR contains information about the subsurface heterogeneities (Thompson & Gist 1993; Haines & Pride 2006; Warden *et al.* 2013; Zyserman *et al.* 2015, 2017; Munch & Zyserman 2016; Gao *et al.* 2017b; Monachesi *et al.* 2018a, b). There are several scenarios of geophysical interest involving non-porous solid media and porous media partially or fully saturated by an electrolyte. Examples are glacial systems, where the upper ice body is modelled as an elastic medium and the rock substrate as a poroelastic medium. In this case, the seismoelectric method provides information about the subglacial pore fluid (Kulessa *et al.* 2006; Monachesi *et al.* 2018a). Other application scenarios include hydrocarbon reservoirs and hydrological reservoirs, where the reservoir rocks can be modelled as poroelastic media and the basement and seal rock as elastic media (Zhang *et al.* 2019).

In addition to these two types of conversions, a third type called evanescent wave has been theoretically and experimentally studied (Liu *et al.* 2008; Ren *et al.* 2016a, b, 2018; Dzieran *et al.* 2020). This EM field is generated at porous/porous, solid/porous, and fluid/porous interfaces (Hu & Wang 2000; Hu & Liu 2002; Ren *et al.* 2016b; Gao *et al.* 2017b; Wang *et al.* 2020). Its amplitude decays rapidly with the normal distance from the interface where it is originated and consequently can only be detected at short distances from it (Ren *et al.* 2016a). In fact, it is difficult to visualize such signals in porous media where coseismic fields dominate in amplitude. On the other hand, within non-porous media, there is no electrokinetic coupling between mechanical and EM energies, so

© The Author(s) 2023. Published by Oxford University Press on behalf of The Royal Astronomical Society. This is an Open Access article distributed under the terms of the Creative Commons Attribution License (https://creativecommons.org/licenses/by/4.0/), which permits unrestricted reuse, distribution, and reproduction in any medium, provided the original work is properly cited.

Downloaded from https://academic.oup.com/gji/article/236/1/62/7328943 by guest on 22 January 2024

no coseismic fields are present. Therefore, evanescent waves can be easily identified in the electric field records and their amplitudes are the strongest at short distances from the interface. Furthermore, Ren *et al.* (2016b) showed the sensibility of the evanescent waves to pore fluid viscosity and salinity variations. These EM waves, also referred as quasi-coseismic fields, were observed as coherent noise in field seismoelectric surveys (Butler 1996; Dupuis *et al.* 2007; Butler *et al.* 2018). Conceptually, they are described as similar to the fringing field outside the edges of a parallel plate capacitor (Butler *et al.* 2018). However, the generation mechanism of evanescent waves is still a matter of current research.

There are several works that simulate the seismoelectric response of different media using numerical methods (Haartsen & Pride 1997; Haines & Pride 2006; Hu *et al.* 2007; Zyserman *et al.* 2010; Gao *et al.* 2019; Zhang *et al.* 2019; Rosas-Carbajal *et al.* 2020). Understanding the generation mechanism of the different types of conversions based on the results of such algorithms, could often be a difficult task. Moreover, numerical methods frequently have the disadvantage of being computationally expensive. However, as we prove in this paper, the main characteristics of the seismoelectric conversions in an elastic/poroelastic interface can be fairly well modelled by means of a simple phenomenological approach with a minimum computational cost.

Several geophysical studies employ a phenomenological perspective (Mavko *et al.* 2009; Warden *et al.* 2013). Generally speaking, a phenomenological approach is a scientific model that represents the global behaviour of a system without considering each component contributions in a formal way (Chisari *et al.* 2018). In other words, it is not the result of solving the governing equations of the considered phenomenon; instead, it is based on a more or less simple physical model that captures the prevailing effects of the studied phenomenon. Despite its simplicity, it provides a fast way to faithfully represent a phenomenon that normally requires a major effort to be studied from the theory. Widely known examples of such models are the ones derived by the linear viscoelastic theory of rock physics, where the mechanical behaviour of rocks is modelled with different configurations of springs and viscous dampers (Burgers 1935; Backus & Mulcahy 1976). Other examples can be found in Rasolofosaon (2009), where different effects in rocks as dispersion, anisotropy, and nonlinearity are represented through a unified model; and in Yan & Vernik (2021), who addressed the study of transversely isotropic medium using phenomenological relations between different stiffness coefficients. In the seismoelectric/electroseismic study field, having a simple model to represent the physical response of heterogeneous systems provides considerable advantages for both modelling (e.g. Monachesi *et al.* 2018a, b; Thompson *et al.* 2023) and inversion (e.g. Guan *et al.* 2013; Macchioli-Grande *et al.* 2020). Principally, as it is shown in this work, it provides a different perspective to understand the physical phenomenon under study. Also, it gives a way to visualize the signals that should be recorded with receivers located at different positions and thus, acquisition arrays can be designed in a more efficient way. This contributes to the study of geophysical scenarios such as glacial systems, hydrocarbon reservoirs, and confined aquifers, among others.

We build the phenomenological approach presented in this paper based in previous works, where the amplitude distribution of the IR generated at a horizontal interface is represented by that of an oscillating vertical dipole centered at the interface, and located right below the seismic source (Thompson & Gist 1993; Pride & Haartsen 1996; Garambois & Dietrich 2002; Warden *et al.* 2012; Smeulders *et al.* 2014; Grobbe *et al.* 2020). Here, we assume that every point on the interface intersected by the wave front radiates as a dipole oriented according to the angle of incidence at that point, during the time the wave front crosses the interface. The formulation of this approach is mathematically similar to the one used to model seismic reflections derived from Kirchhoff theory (Hilterman 1975). We validate our proposal by comparing the response of the phenomenological model with that of an already known finite-element-based code that computes the seismoelectric response in different scenarios (Zyserman *et al.* 2010, 2012, 2022), as it is detailed in the following section.

2 THE SEISMOELECTRIC PHENOMENOLOGICAL MODEL

Consider a dielectric medium Ω (Figs 1b and d) where we aim to compute the EM response of the seismoelectric phenomenological model (SPM). Simultaneously, consider a perfectly elastic medium Ω_E overlying a poroelastic one Ω_P (Figs 1a and c). Due to the deployment of a seismic source in Ω_E, seismic and seismically induced EM responses are triggered in $\Omega_E \cup \Omega_P$. Our objective is to approximate the EM signals in Ω_E through the SPM. This model assumes that EM fields are generated in Ω by sources acting at times and positions where the seismic wave front intersects the interface Γ_{EP} in $\Omega_E \cup \Omega_P$. In particular, we assume that each contributing EM field in Ω is produced by an electric dipole oriented according to the angle of incidence of the wave front on the interface Γ_{EP} (Fig. 1). The time lapse during which each dipole is active is equal to the time the wave front takes to cross the interface through such point. Therefore, every point in the interface will start to radiate in Ω at different times coincident with the arrival times of the seismic wave front to Γ_{EP}. As a result, the total modelled EM response (i.e. the SPM response) will be the linear superposition in space and time of each dipolar field. Note that, following Pride's (1994) theory, no seismic-to-EM energy conversion is produced in the elastic medium due to the absence of fluid, before any wave front arrives at the interface. Therefore, no coseismic fields are considered in our approach. As mentioned in the Introduction, the ideas on which this model is based were motivated by different works characterizing the radiation pattern of the IR as an oscillating vertical electric dipole. In some of these studies, it is shown that the area that contributes to the IR generation is the first Fresnel zone at the respective interface. Following this description and as an extension, this phenomenological approach proposes that every point (and not only those that constitute the first Fresnel zone) of the interface excited by the seismic wave, will radiate as dipoles. We will show that the results obtained with our SPM not only verify Garambois' descriptions for the IR (Garambois & Dietrich 2002), but also can explain the nature of the evanescent waves.

To further explain our model, let us now suppose that a seismic wave front with a given time signature arrives at the interface of the heterogeneous medium $\Omega_E \cup \Omega_P$ at time t_0 and position P_0^1 (Fig. 1a). At these very moment and position, the first dipole is activated in the homogeneous medium Ω with a vertical orientation (Fig 1b). Later, at a time $t_0 + \mathrm{d}t$, the seismic wave front impinges in another positions P_0^j and P_0^k of the interface (Fig. 1c), symmetrically located with respect to P_0^1. In the same way, another two dipoles are activated at that moment and positions, with an orientation given by the incidence angle of the wave front at such positions, and with a lower amplitude than that of the first dipole due to the geometrical spreading of the wave front (Fig. 1d). Likewise, contiguous pairs of dipoles are activated successively in Ω simulating the EM response

Downloaded from https://academic.oup.com/gji/article/236/1/62/7328943 by guest on 22 January 2024

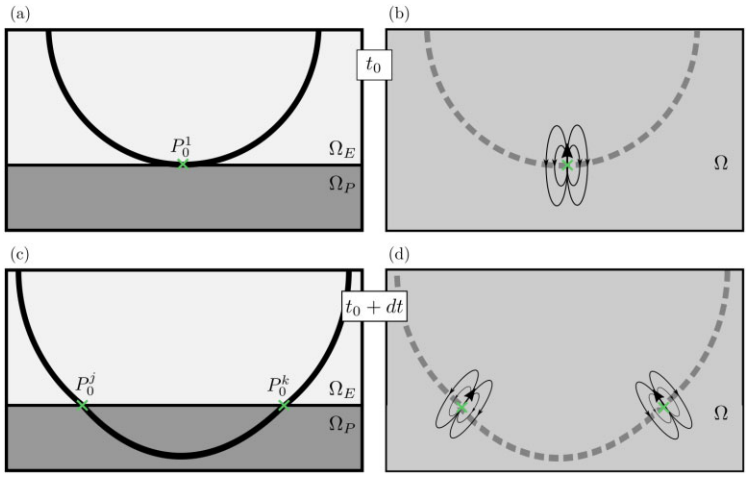

Figure 1. The EM response of the interface between Ω_E and Ω_P in (a) and (c) is modelled with a set of contiguous vertical electric dipoles in a homogeneous medium Ω in (b) and (d) that are activated successively at the times and positions in which the seismic wave intersects the interface. In (a) and (b), $t = t_0$ represents the first arrival time and consequently it is the activation time of the first dipole in P_0^1. Later, at $t = t_0 + \mathrm{d}t$ (in (c) and (d)) the wave arrives at two points P_0^j and P_0^k of the interface, thus at this moment two dipoles symmetrically located with respect to P_0^1 are simultaneously activated.

generated by seismic-to-EM conversions at the interface in the heterogeneous medium. The time interval during which each dipole is active coincides with the passage of the seismic wave through the corresponding point of the interface.

In order to build the analytical expression for the proposed model we consider, following Garambois & Dietrich (2002), the electric field generated by a static electric dipole; note that in the present approach we restrict ourselves to a 2-D geometry. So, we compute the electric field $\boldsymbol{E_d}$ created by two infinitely long wires (transverse to the x–z plane) with linear charge density $+M_0$ and $-M_0$ (hereafter referred to as dipoles):

$$\boldsymbol{E_d} = \frac{M_0}{2\pi\epsilon_0}\left[\frac{\hat{\boldsymbol{r}}_1}{r_1} - \frac{\hat{\boldsymbol{r}}_2}{r_2}\right]. \tag{1}$$

Here $\boldsymbol{r}_1$ and $\boldsymbol{r}_2$ are the vectors pointing from the respective charged lines to the point of the plane $P = (x, z)$ where $\boldsymbol{E_d}$ is computed, and ϵ_0 is the vacuum electric permittivity. In addition, for each dipole i we must include an activation time τ^i and a temporal dependence.

If we consider a finite distribution of N dipoles centred at positions $P_0^i = (x_0^i, z_0^i)$ activated at different times $\tau^i, \forall i = 1, \ldots, N$ and with charge density M_0^i, then the total electric field is:

$$\boldsymbol{E}(P, t) = \sum_{i=1}^{N} \boldsymbol{E_d}(P, P_0^i, t, \tau^i, M_0^i). \tag{2}$$

In eq. (2), we consider that the dipoles have the same orientation as the incident seismic wave. Furthermore, for successive times corresponding to a seismic wave hitting the interface, assuming that the latter can be parametrized as $z(x_0^i)$, the activation time τ^i depends only on the offset x_0^i, that is, $\tau^i = \tau(x_0^i)$. In order to include the geometrical spreading effect of the cylindrical seismic wave front, we assume that M_0^i decays with the distance to the source r^i according to $M_0^i = M_0/\sqrt{r^i}$ (Wang *et al.* 2000). Note that $r^i = \sqrt{[x_s - x_0^i]^2 + [z_s - z_0(x_0^i)]^2}$, where (x_s, z_s) is the source location. Note, then, x_0^i is the only remaining free variable in eq. (2) that is modified for each dipole. If we consider a horizontal infinite line of vertical 2-D dipoles along the x–z plane, we have that the

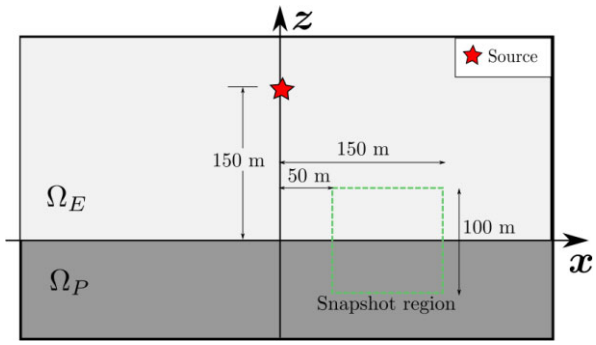

Figure 2. Representation of the 2-D heterogeneous model, composed by an elastic layer Ω_E over a poroelastic half-space Ω_P. A Cartesian coordinate system was adopted, with the x-axis located at the interface and the z-axis pointing upwards with the origin in the interface. The star represents the source and the green box the region were the snapshots are taken.

total electric field is:

$$\boldsymbol{E}(P, t) = \int_{-\infty}^{+\infty} \boldsymbol{E_d}(P, t, x_0)\mathrm{d}x_0. \tag{3}$$

Let us assume that $\mathcal{F}(t)$ represents the temporal signature of the dipoles. For a compressional point source located at zero offset (according to the coordinate system adopted in Fig. 2) and a horizontal interface, the activation time τ and the offset are related by

$$\tau = \sqrt{t_0^2 + (x_0/v)^2}, \tag{4}$$

where $t_0 = H/v$, H is the vertical distance between the source and the interface and v is the seismic compressional velocity of the medium Ω_E. Note that through eq. (4) τ is related with the so-called 'wave front sweep velocity' indicating the rate at which the wave front intersects the interface (Hilterman 1975). Associated with this source, the first dipole is activated at zero offset and time t_0, and the remaining dipoles are activated successively in pairs symmetrically with respect to the zero offset. Consequently, the activation time increases with the offset. In summary, the analytical expression for the SPM is given by:

$$\boldsymbol{\mathcal{E}}^{\mathrm{tot}}(P, t) = \int_{-\infty}^{\infty} \boldsymbol{E_d}(P, x_0)\mathcal{F}(t - \tau(x_0))\mathrm{d}x_0. \tag{5}$$

Downloaded from https://academic.oup.com/gji/article/236/1/62/7328943 by guest on 22 January 2024

Table 1. Physical properties of the poroelastic half-space.

Solid grain bulk modulus K_s, [GPa]	36	Fluid bulk modulus K_f, [GPa]	2.2
Solid grain shear modulus G_s, [GPa]	45	Fluid viscosity η, [Pa·s]	0.001
Solid grain density ρ_s, [kg m^{-1}]	2600	Fluid density ρ_f, [kg m^{-1}]	1000
Compressional wave velocity V_P, [m s^{-1}]	1837	Fluid salinity C_0, [mol L^{-1}]	0.002
Shear wave velocity V_S, [m s^{-1}]	600	Porosity ϕ	0.25

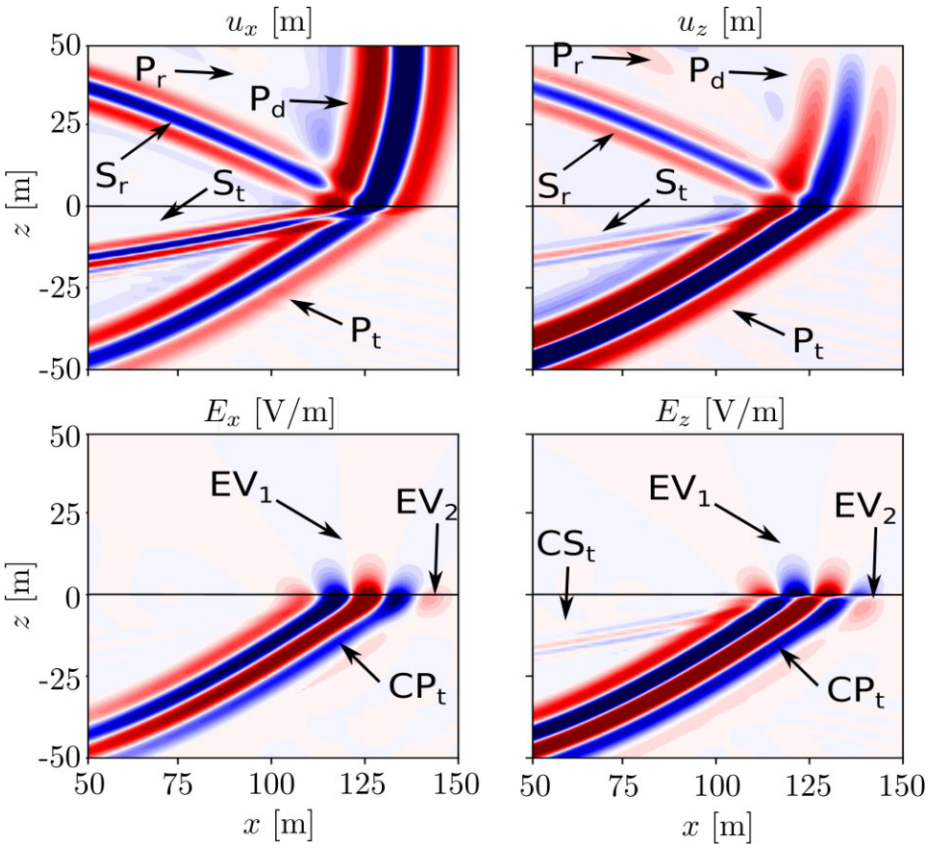

Figure 3. Seismic (upper panels) and electric (bottom panels) field snapshots for the elastic/poroelastic system, in both horizontal (left) and vertical (right) components and in the subdomain [50 m, 150 m] × [−50 m, 50 m], calculated with the PSVTM code. The displacement fields show the direct P_d, reflected P_r, and transmitted P_r compressional waves, as well as the reflected S_r and transmitted S_t shear waves. The observable electric field signals are evanescent waves on both sides of the interface (EV_1 and EV_2) and coseismic compressional CP_t and shear CS_t fields on the poroelastic side.

As a remarkable feature, the SPM can be constructed taking into account just the compressional velocity of the upper elastic layer and the vertical distance between the source and the interface. This means that it does not depend on the underlying poroelastic physical properties (we will expand this in Section 4). In the next section, we present and detail the seismoelectric response obtained with the PSVTM (compressional *P* and vertical shear *SV* waves coupled with the transverse-magnetic) code, and their comparison with the one obtained with the SPM.

3 RESULTS

This section is divided into two parts. First, we show and analyse results obtained with the PSVTM code, with special emphasis on the radiation pattern of the electric fields as a function of the distance to the interface. After that, we validate the results of the proposed SPM computed with eq. (5) by comparing them with the former. For this, we consider three geological scenarios: the first one (model A), consists of a perfectly elastic horizontal layer Ω_E overlying a poroelastic half-space Ω_P; the second one (model B) comprises a horizontal porous layer positioned between two elastic layers. The upper elastic layer has a finite thickness, while the lower layer extends into a semi-space. The third model (model C) is similar to model A with the difference that the interface between both media is a curved line.

3.1 Seismoelectric PSVTM response

The mentioned code solves the decoupled 2-D Pride's equations governing the seismoelectric phenomenon through numerical algorithms based on a finite-elements procedure (Zyserman *et al.* 2020). In this code, solutions to both Biot's equations and Maxwell's equations (with seismically induced sources) are approximated by means of mixed finite elements, employing a naturally parallelizable domain decomposition technique. Note that the numerical approach for the seismic component of the algorithm can straightforwardly deal with the elastic/poroelastic case, just by considering a negligible porosity for the elastic region; this approach has also been

Downloaded from https://academic.oup.com/gji/article/236/1/62/7328943 by guest on 22 January 2024

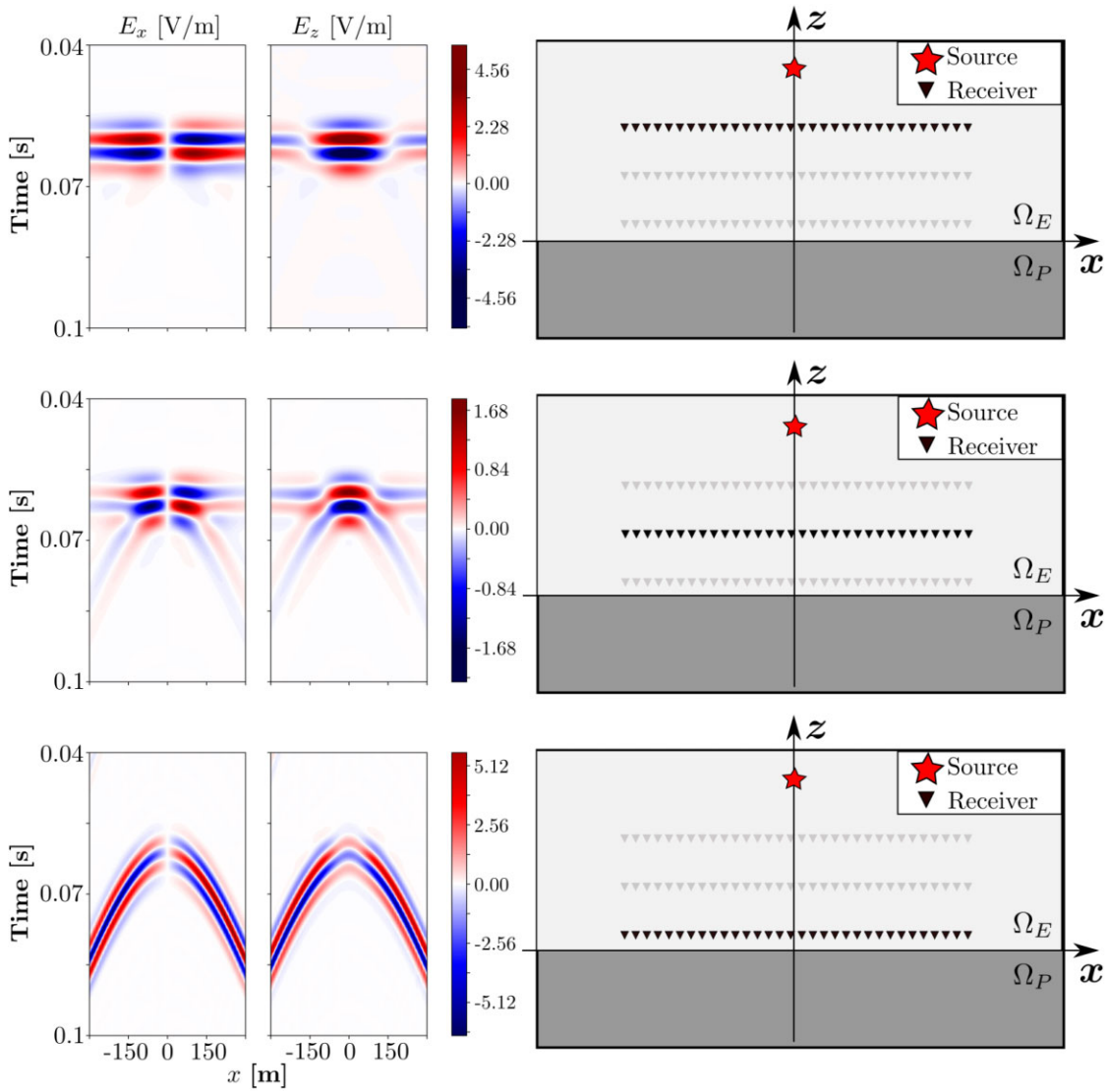

Figure 4. Seismoelectric response calculated with the PSVTM code: x and z electric field components recorded on three receiver lines located at $z = 100$, 50 and 5 m of the interface. A clear horizontal event centered at approximately $t = 0.06$ s is observed for the upper receiver line, associated with the IR. A hyperbolic event associated with the evanescent wave with apex at the same time is observed at the lower receiver line. For the middle receiver line, the amplitudes of both events are approximately of the same order.

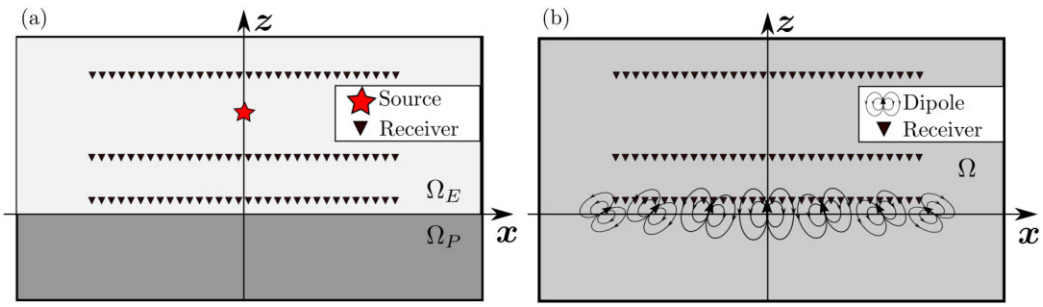

Figure 5. Representation of model A: physical scenario and acquisition geometry for the (a) PSVTM simulations and (b) for the SPM. The heterogeneous medium is composed by an elastic layer Ω_E over a poroelastic half-space Ω_P were the source, represented with the red star, is located at zero offset and $z =$ 50 m. In the homogeneous medium Ω, the dipoles are centred in the x-axis. In both scenarios, three receiver lines are located at $z = 5$, 25 and 75 m (black triangles).

Downloaded from https://academic.oup.com/gji/article/236/1/62/7328943 by guest on 22 January 2024

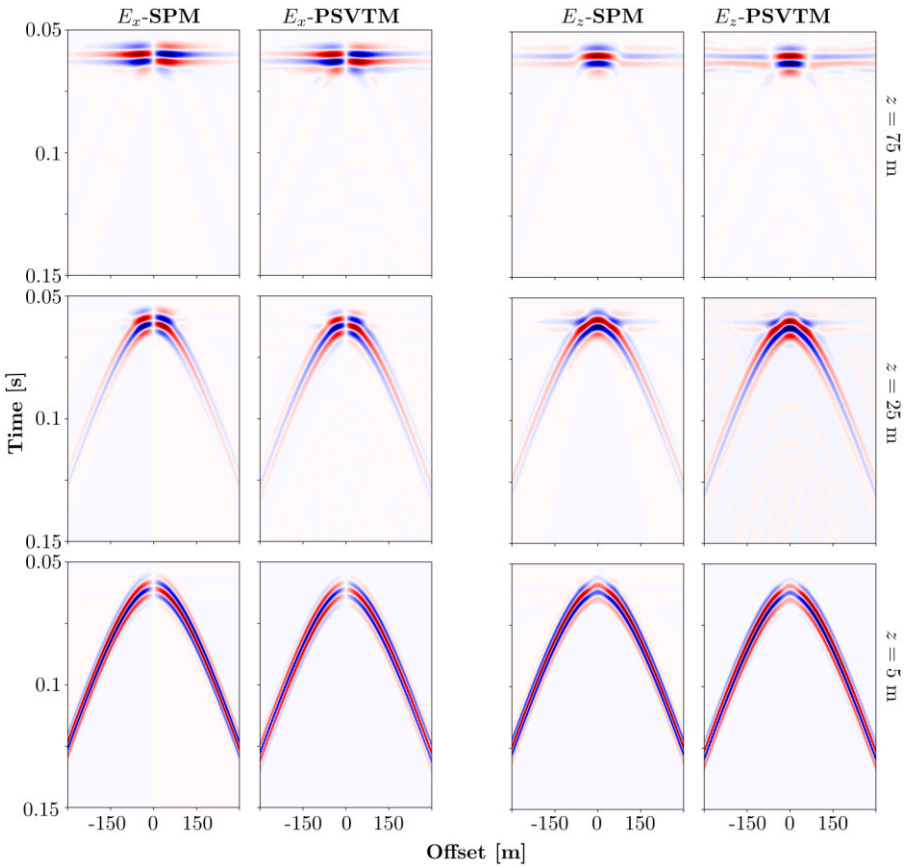

Figure 6. Results for model A: comparison between the SPM gathers (first and third columns) and the PSVTM gathers (second and fourth columns) for E_x (left-hand panels) and E_z (right-hand panels), for different receivers line distance to the interface: $z = 5$ m (upper panels), 25 m (middle panels) and 75 m (bottom panels). The central frequency of the source is 120 Hz. Again, the gathers show the two signals corresponding to the IR and the evanescent wave. With decreasing receivers line distance to the interface, both the SPM and the PSVTM gathers show the amplitude of the IR increasing relative to the evanescent wave amplitude.

employed by other authors (Corredor *et al.* 2014; Zhang *et al.* 2019). For the initial simulations, we consider the physical scenario and acquisition geometry of Fig. 2. This model consists of a 300 m thick elastic layer overlying a water-saturated poroelastic half-space. The z-axis is directed upwards and has its origin at the interface. The properties of the poroelastic medium are listed in Table 1, while the elastic medium has a density of 2600 kg m^{-3} and a compressional wave velocity of 2735 m s^{-1}. We consider a compressional seismic point source within Ω_E, located at $z_s = 150$ m and zero offset, with a time signature given by a Ricker wavelet:

$$\mathcal{G}(t) = [1 - 2\pi^2 f_0^2 (t - t_d)^2] e^{-\pi^2 f_0^2 (t - t_d)^2}, \tag{6}$$

with a central frequency $f_0 = 120$ Hz and a time delay $t_d = f_0^{-1}$.

Snapshots of the seismic fields and the induced electric fields in both vertical and horizontal components are shown in Fig. 3, corresponding to the region [50 m, 150 m] $\times$ [$-$ 50 m, 50 m], which contains a portion of the interface. All snapshots are taken at the same time. On the seismic panels, within Ω_E, the direct P wave arriving at the interface, the reflected P wave and the reflected converted S wave can be observed; while within Ω_P, the transmitted P and S waves are present. Regarding the electric field snapshots, we can clearly observe the coseismic signals accompanying the seismic waves transmitted to the poroelastic medium. The coseismic signal induced by the transmitted S wave is appreciable only in the vertical component. We recall that Ω_E has a higher seismic velocity than Ω_P, thus no critically or post-critically refracted waves are present in the seismic field snapshots, nor coseismic signals accompanying these in the electric field snapshots. It can also be noted that, as expected, within Ω_E coseismic signals induced by seismic waves are not present since no electrokinetic coupling exists in this medium. Instead, we can observe an electric signal in the elastic medium accompanying the arrival of the seismic P wave at the interface. This signal has the characteristic of being strong in the vicinity of the interface, attenuating rapidly with the distance. For this reason, and according to the characterization carried out in previous works (Ren *et al.* 2016a; Dzieran *et al.* 2020), we interpret this signal as the evanescent wave.

A different visualization of the results is depicted in Fig. 4. The horizontal and vertical electric field components were recorded by three horizontal receiver lines, located within the elastic medium at $z = 5$, 50 and 100 m, with offsets ranging between $x = -150$ and 150 m. In these gathers we observe two clear signals whose relative amplitudes change depending on the distance to the interface of the corresponding receiver line. In the records of the top line ($z =$ 100 m), we observe a clear event that arrives simultaneously at all the receivers. We interpret this horizontal event as the IR produced at the interface Γ_{EP}, since the time at which this signal is centred coincides with the time at which the seismic wave first arrives at the interface. On the other hand, in the records of the bottom receiver line located at $z = 5$ m, we can see a hyperbolic event which we interpret as the evanescent wave. This signal is synchronous to the successive arrival times of the direct seismic P wave at Γ_{EP}. Finally,

Downloaded from https://academic.oup.com/gji/article/236/1/62/7328943 by guest on 22 January 2024

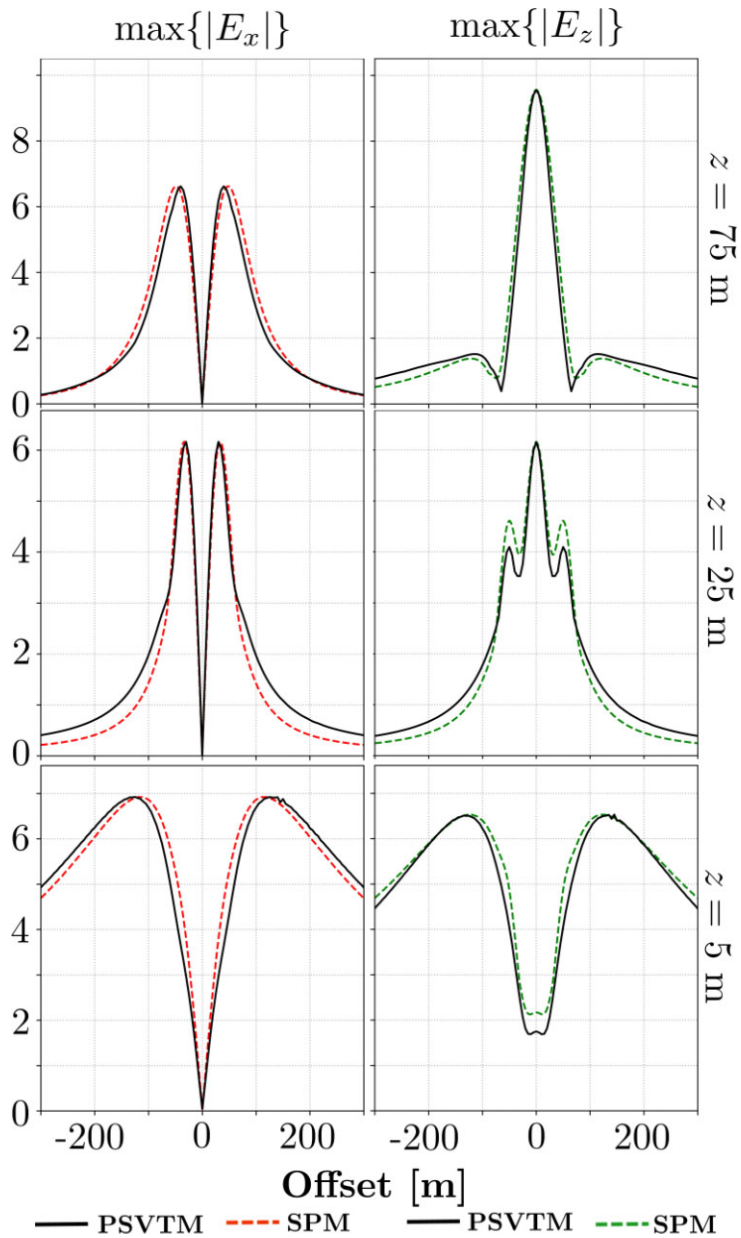

Figure 7. Results for model A: comparison between the SPM and the PSVTM for the maximum values of $|E_x|$ and $|E_z|$ for each individual trace and for offsets between -300 and 300 m. The upper panels corresponds to the receiver line located at $z = 75$ m, the middle panels to $z = 25$ m and the bottom panels to $z = 5$ m. The central frequency of the source is 120 Hz.

the receivers corresponding to the middle line ($z = 50$ m) show both events with approximately the same amplitude. We note that the IR signal is centred at a time approximately coincident with that of the evanescent wave apex. This is what we expected to see, since both are generated from the moment the seismic wave arrives at Γ_{EP}. We conclude this analysis mentioning that the behaviour of the seismoelectric response obtained with the PSVTM code is consistent with that already published by Ren *et al.* (2016a, 2018).

3.2 Comparison between SPM and PSVTM code responses

In order to evaluate the capabilities of the SPM, we perform several comparisons between its response and the one obtained with the 2-D PSVTM code. We compute the SPM response in a homogeneous medium Ω (Fig. 5b) from eq. (5). The integral was numerically approximated by means of a quadrature rule using a spatial sampling Δx_0 equal to 1 m. Our tests indicate that smaller samplings does not produce appreciable changes to the global response. For the source time signature, we choose the derivative of a Ricker wavelet:

$$\mathcal{F}(t-\tau) = -2\pi^2 f_0^2 (t-\tau)[3 - 2\pi^2 f_0^2 (t-\tau)^2] e^{-\pi^2 f_0^2 (t-\tau)^2}, \quad (7)$$

where τ has the dependence on the offset given by eq. (4) and f_0 is set to 120 Hz. Meanwhile, for the PSVTM simulations, we maintain the physical scenario $\Omega_E \cup \Omega_P$ presented in Fig. 2 (defined as model A) and the source time signature, only changing the source distance to the interface to $z = 50$ m (Fig. 5a).

We record the electric fields in three receiver lines, located at $z =$ 5, 25 and 75 m with offsets ranging between $x = -300$ and 300 m (see Fig. 5). Note that for the scenario of the SPM, the value of

Downloaded from https://academic.oup.com/gji/article/236/1/62/7328943 by guest on 22 January 2024

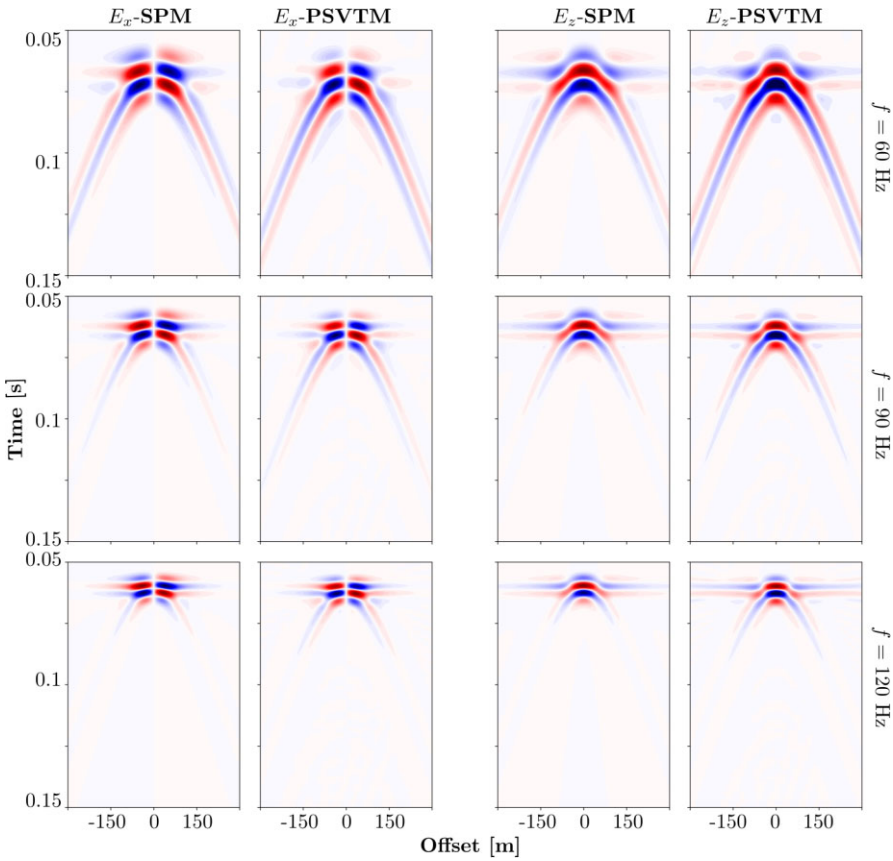

Figure 8. Results for model A: comparison between the SPM gathers (first and third columns) and the PSVTM gathers (second and fourth columns) for E_x (left-hand panels) and E_z (right-hand panels), for different source central frequencies: $f = 60$ Hz (top panels), $f = 90$ Hz (middle panels) and $f = 120$ Hz (bottom panels). The receivers line is located at $z = 50$ m. All the gathers show an horizontal signal centred at 0.06 s approximately and zero offset (IR), and a second hyperbolic arrival with an apex centred in the same position (evanescent wave). With increasing frequency and offset, both SPM and PSVTM gathers show the evanescent wave amplitude decrease.

the z coordinate represents the normal distance between the dipoles and the receiver line. On the other hand, we also notice that for visualization purposes the results are normalized so that in each gather the maximum amplitude of both approaches coincide. In Fig. 6, we observe that the captured radiation patterns for the three receiver lines display the same characteristics for both responses. As detailed previously for the PSVTM case, the SPM response also consists of a horizontal event far from $z = 0$, a hyperbolic event near $z = 0$ and the co-existence of the two at an intermediate height. This is to say that near the dipoles the superposition of the dipolar EM fields results in a radiation pattern displaying a hyperbolic geometry, so it is naturally identifiable as the evanescent wave. Conversely, away from the dipoles the superposition yields a horizontal pattern which can naturally be identified as the IR. In summary, all the mentioned characteristics of the seismoelectric response obtained with the SPM are coincident with the ones computed with the PSVTM code. This comparison shows an excellent agreement between the radiation patterns of both approaches.

In Fig. 7, we show the maximum absolute values of the electric field components ($\max\{|E_x|\}$ and $\max\{|E_z|\}$), for the three receiver lines set in model A. In this figure, the amplitude curves for both vertical and horizontal electric field components yielded by both approaches are compared for each receiver line. As expected, for the panels corresponding to the receiver line located at $z = 75$ m (upper panel), the amplitude curves present a dipolar behaviour, consistent with the IR characteristics. On the other hand, the amplitudes corresponding to the receiver lines located at $z = 25$ and 5 m (middle and bottom panels of Fig. 7) exhibit more complex patterns. Again, the similarities between the SPM and PSVTM curves are remarkable. From the top panels, we observe the SPM results slightly stretched in the offset direction with respect to the PSVTM ones. In the middle panels, this stretching is negligible and the main differences are in the amplitudes of the computations, especially at ± 40 m offset for the vertical component. Finally, from the bottom panels, we observe again a small stretching but inverted with respect to the top panels: the PSVTM is elongated in the offset direction. We deem that the differences between both results are due to the fact that the SPM does not take into account the properties of the poroelastic medium, nor the inductive effects.

Fig. 8 shows comparisons between electric field records where different central source frequencies for the time signatures for the dipolar fields in the SPM and for the seismic wave front in the PSVTM code are considered. We set $f_0 = 60$, 90 and 120 Hz which are within the range of shallow seismoelectric surveys (10 Hz–1 kHz, Haines & Pride 2006; Bordes *et al.* 2015; Gao *et al.* 2017a; Guan *et al.* 2017). The receiver lines are located at $z = 50$ m in Ω and Ω_E, respectively. On the one hand, in the PSVTM code results we note that the evanescent wave becomes stronger than the IR as f_0 decreases. This amplitude increase is consistent with the descriptions provided by Ren et al. (2018). On the other hand, the SPM successfully captures this behaviour; for a given central frequency

Downloaded from https://academic.oup.com/gji/article/236/1/62/7328943 by guest on 22 January 2024

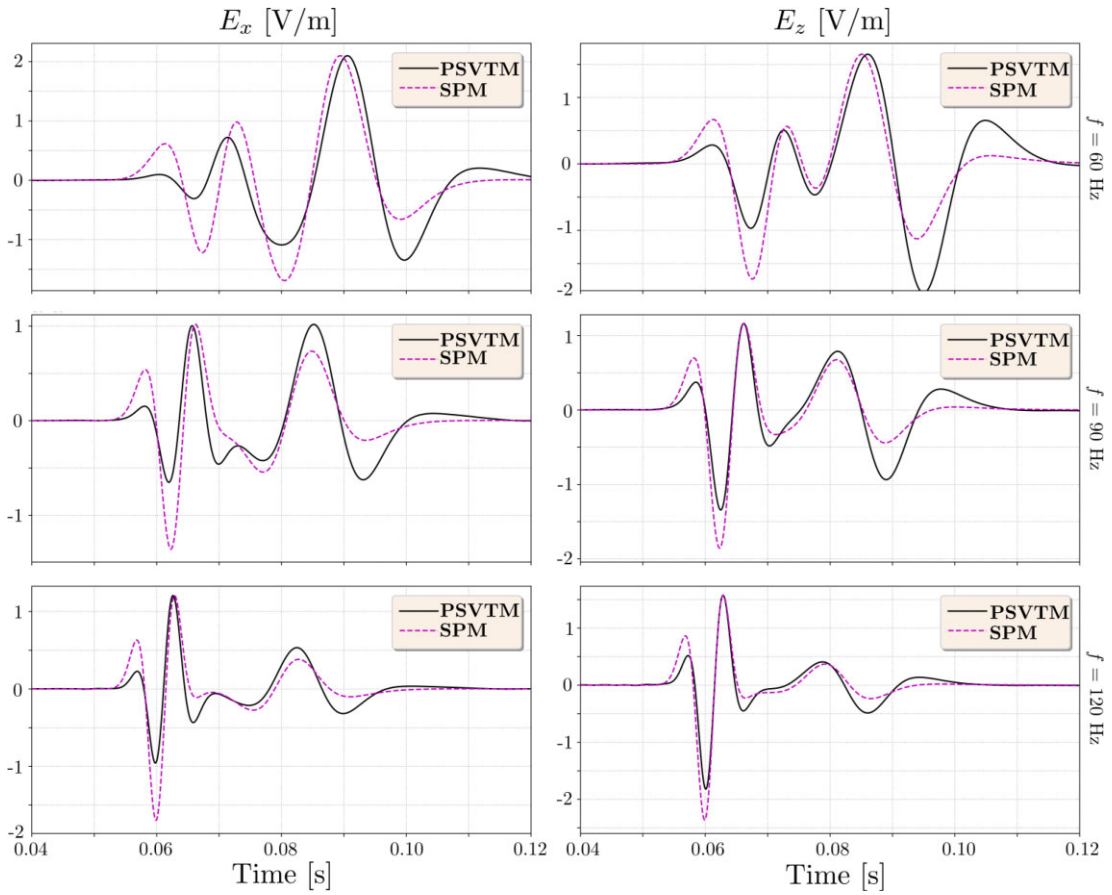

Figure 9. Results for model A: comparison between individual traces for E_x (left-hand column) and E_z (right-hand column) of the PSVTM (solid curves) and the SPM (dotted curves) at a source central frequency of 60 Hz (top panels), 90 Hz (middle panels) and 120 Hz (bottom panels). The receiver distance to the interface is 50 m and the offset is 150 m in all cases.

of the source, the IR is produced only by the dipoles located near the zero-offset (Garambois & Dietrich 2002) and thus, the individual dipolar fields interfere in a constructive way. Conversely, the evanescent waves are created by the dipoles located at higher offsets, so the differences in the activation times between successive dipoles increases due to the geometry of the wave front, which results in a less constructive interference of these dipolar fields. This explains the higher amplitudes exhibited by the IR with respect to the evanescent waves and why this amplitude difference increases for higher central frequencies of the source.

Fig. 9 shows comparisons between individual traces of the two components of the electric field extracted from the gathers for both approaches presented in Fig. 8. They correspond to the receivers located at $x = 150$ m in Ω_E and Ω. To study the amplitude ratio between the evanescent wave and the IR signal, it is necessary to consider far offsets such as the former arrives at later times than the latter so that they can be observed separately in a single temporal electric field record. Also, we must consider an intermediate height of the receiver line, in order to capture both conversions with detectable amplitude. As can be observed for the frequencies considered, the SPM response represents fairly well the amplitude ratio between the IR (first arrival in the traces) and the evanescent wave (second arrival) obtained with the PSVTM code. The traces corresponding to the lower frequency (60 Hz) show the evanescent wave as the strongest event; for the traces corresponding to 90 Hz, both events presents a similar amplitude, and for 120 Hz, the IR exhibit a higher amplitude than the evanescent wave. Again, this verifies the hypothesis that for lower source central frequencies, the evanescent wave has a higher relative amplitude due to higher constructive interference.

In order to test the flexibility of the SPM, we perform a sensibility analysis by modifying in the PSVTM code the porosity and fluid salinity (which in turn modifies the medium conductivity) of the poroelastic half-space, considering a source central frequency of 120 Hz. Figs 10 and 11 show the same type of comparison as Fig. 9 (i.e. overlapped individual records of receivers located at $x = 150$ m and $z = 50$ m). As mentioned before, no modifications need to be applied to the SPM, since it is not dependent on the poroelastic properties. Again, it can be observed that the SPM approximately preserves the relative amplitudes between the IR and the evanescent signals. In other words, this result seems to indicate that there is only one physical process taking place at the interface and originating both signals. Obviously, the absolute amplitudes are dependent on these properties, since, for example, a null porosity results in a non-existent seismoelectric response. However, as can be seen from these results, the radiation pattern remains approximately the same for different values of the parameters.

The analysis performed in this section involving the results of Figs 7–11 displays the ability of the SPM to capture the complete seismoelectric response, which has the same characteristics as those outlined in previous works by employing numerical simulations (Ren *et al.* 2016a, b, 2018; Dzieran *et al.* 2019).

We now consider model B, where we set the thickness of the poroelastic layer equal to 30 m and the seismic source at $z = 50$ m,

Downloaded from https://academic.oup.com/gji/article/236/1/62/7328943 by guest on 22 January 2024

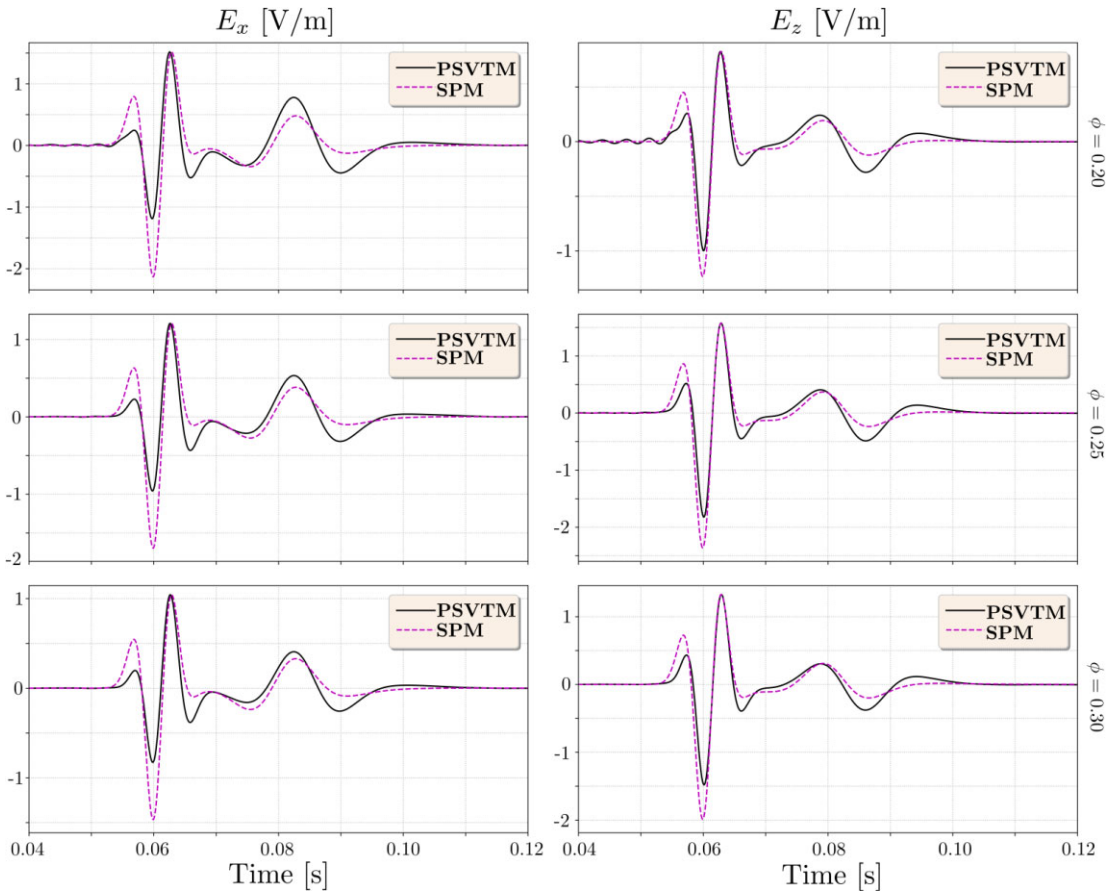

Figure 10. Results for model A: comparison between individual traces for E_x (left-hand column) and E_z (right-hand column) of the PSVTM (solid curves) and the SPM (dotted curves) for porosities of 0.2 (top panels), 0.25 (middle panels) and 0.3 (bottom panels). The receiver distance to the interface is 50 m and the offset is 150 m in all cases. The central frequency considered is 120 Hz.

see Fig. 12. When applying the SPM for this geometry, we consider two different dipole lines located at the top and bottom of the poroelastic layer, respectively. The first dipole in the topmost line is activated when the direct P wave hits the topmost interface, and like in the previous model, the adjacent dipoles are activated sequentially. The first dipole in the bottom line is activated at the moment in which the transmitted P wave hits the top boundary of the elastic semi-space; the adjacent dipoles are likewise sequentially activated. Note that here both the elastic and poroelastic seismic velocities must be considered for the activation times of the first and second dipole lines, respectively. Finally, the first line of dipoles is again activated when the upward travelling reflected seismic wave impinges in the topmost interface. We are not considering any other reflections due to the time length of the considered traces. Fig. 13 shows a comparison between the SPM and the PSVTM responses for two receivers lines located at $z = 75$ m (upper panels) and $z = 25$ m (bottom panels). In the records of the first line, we observe three horizontal events centred approximately at $t = 0.02$, 0.04 and 0.06 s which we interpret as the IRs generated at the interfaces, corresponding to the seismic wave impinging in the top, bottom and again top boundaries of the poroelastic layer, respectively. In the records of the second receivers line (bottom panels), we also observe the respective evanescent waves accompanying each IR and as expected, the first one is the strongest. The second evanescent wave is weaker than the others due to the seismic energy loss in the second elastic half-space. Fig. 14 shows individual traces of these gathers corresponding to 30 m offset. Again we observe that the SPM captures fairly well the waveforms and relative amplitudes of the electric signals, indicating its capability to handle also layered subsurface geometries with a fairly small amount of added complexity.

Finally, we consider model C (Fig. 15), which is identical to model A but with a convex curved interface. This geometry is present in tectonic extensional regimes involving detachment faults. In this case, the dipole orientation changes for every point on the interface. In addition, the activation times of each dipole will respond to the arrival time of the seismic wave at this interface, which is given by:

$$\tau = \frac{\sqrt{(z_s - z)^2 + x_0^2}}{v}, \tag{8}$$

where z is the interface vertical coordinate, which was fixed to $z = -35$ m at zero offset and z_s is set to 70 m. Results of the computations of the PSVTM code and the SPM for this scenario can be seen in Fig. 16. This figure shows records from two receiver lines located at $z = 25$ m (upper panels) and $z = 5$ m (lower panels), with offsets ranging between -150 and 150 m for both components. In both lines, the IR can be observed as a horizontal event centred approximately at $t = 0.045$ s and the evanescent wave, with their characteristic hyperbolic behaviour. As we observe, the amplitudes of the latter are higher for negative offsets than for positive offsets. This is what we expected since this region is closer to the interface compared to the region of positive offsets. Comparing with the

Downloaded from https://academic.oup.com/gji/article/236/1/62/7328943 by guest on 22 January 2024

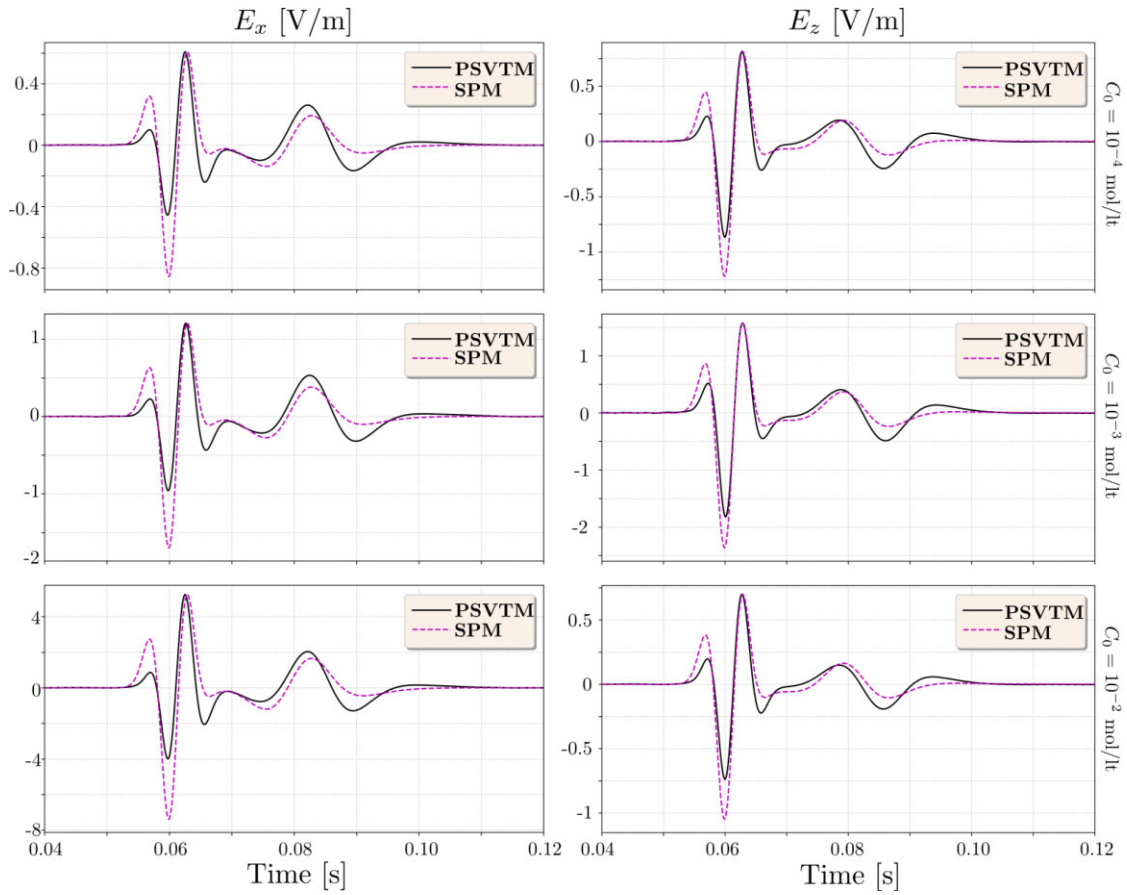

Figure 11. Results for model A: comparison between individual traces for E_x (left-hand column) and E_z (right-hand column) of the PSVTM (solid curves) and the SPM (dotted curves), for fluid salinities of 10^{-4} mol L^{-1} (top panels), 10^{-3} mol L^{-1} (middle panels) and 10^{-2} mol L^{-1} (bottom panels). The receiver distance to the interface is 50 m and the offset is 150 m in all cases. The central frequency considered is 120 Hz.

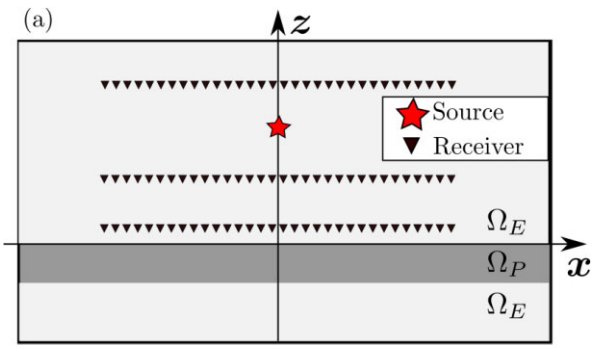

Figure 12. Representation of model B, composed by a 30 m thick poroelastic horizontal layer Ω_P set between two elastic half-spaces Ω_E. The first interface is located at $z = 0$ ant the second at $z = -30$ m. The source and receiver locations are the same of those considered in model A.

results of the PSVTM code, it is interesting to note how the SPM represents the amplitude patterns of the electric fields. Fig. 17 shows individual traces of the records in Fig. 16 in horizontal and vertical components, corresponding to a -30 m offset. Again we highlight the fact that the SPM reproduces the amplitude ratio and waveforms of the electric signals. In this way, we prove the SPM applicability to non-horizontal interfaces.

4 DISCUSSION

When formulating the SPM, we introduced several simplifying assumptions that should be discussed. We start by mentioning that the absolute amplitudes of the seismoelectric conversions have not yet been described. Although it would be expected that these amplitudes depend on the contrast in mechanical and EM properties between both media, this should be validated through the computation of the corresponding reflection and transmission coefficients for an incident seismic wave at the interface. This means to analytically solve the EM/mechanical equations given by Pride (1994) in a coupled elastic/poroelastic medium, a task that is beyond the scope of this paper. These reasons probably explain the main differences between the models, and trigger questions that motivate forthcoming studies. In this way, we propose to study the seismoelectric conversions and validity of the SPM taking place at interfaces involved in other physical scenarios. For example, we are interested in the acoustic/poroelastic case with non-horizontal and irregular interfaces, which has several geophysical applications.

Regarding the considered 2-D geometry, we argue that an extension to 3-D could be straightforwardly considered. A compressional seismic point source will create a spherical wave front that can be treated in the same way as the cylindrical wave front in a 2-D geometry. In this case, expressions for the electric field created by two point charges of different sign or by the well-known expression for

Downloaded from https://academic.oup.com/gji/article/236/1/62/7328943 by guest on 22 January 2024

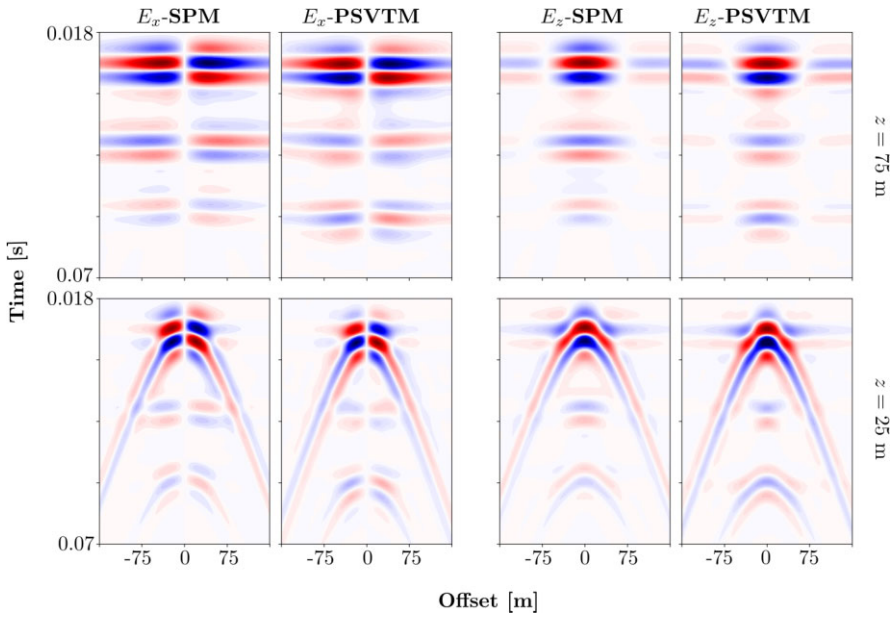

Figure 13. Results for model B: comparison between the SPM gathers (first and third columns) and the PSVTM gathers (second and fourth columns) for E_x (left-hand panels) and E_z (right-hand panels), for different receivers line distance to the interface: $z = 5$ m (upper panels), 25 m (middle panels) and 75 m (bottom panels). The central frequency of the source is 120 Hz. Again, the gathers show the two signals corresponding to the IR and the evanescent wave. With decreasing receivers line distance to the interface, both the SPM and the PSVTM gathers show the amplitude of the IR increasing relative to the evanescent wave amplitude.

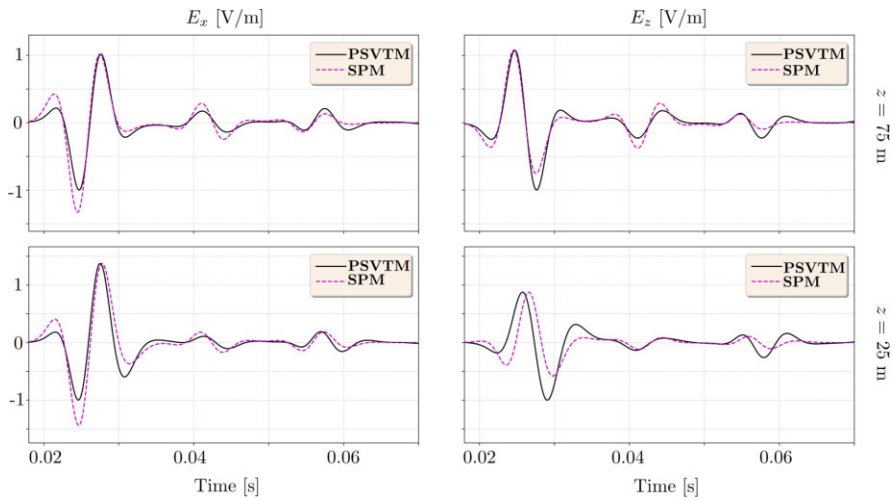

Figure 14. Results for model B: comparison between individual traces for E_z of the PSVTM (solid curves) and the SPM (dotted curves) at a source central frequency of 120 Hz. The receiver distance to the interface is 25 m (upper panel) and 5 m (bottom panel) and the offset is −90 m in both cases.

the point electric dipole could be employed instead of eq. (1) at each point of a spreading circumference:

$$\mathcal{E}^{\text{tot}}(P, t) = \int_S \boldsymbol{E_d}(P, \boldsymbol{r_0})\mathcal{F}(t, \boldsymbol{r_0})\mathrm{d}S, \tag{9}$$

where $\boldsymbol{E_d}$ is the expression for the 3-D electric field generated by two point charges q and $-q$ at positions $\boldsymbol{r_1}$ and $\boldsymbol{r_2}$:

$$\boldsymbol{E_d} = \frac{q}{4\pi\epsilon_0}\left(\frac{\hat{\boldsymbol{r}}_1}{r_1^2} - \frac{\hat{\boldsymbol{r}}_2}{r_2^2}\right), \tag{10}$$

S is the area representing the intersection between the 3-D wave front and the interface. Meanwhile, $\boldsymbol{r_0}$ contains the dependence between the location of the dipoles and their respective activation times. We argue that the results for the 3-D case will be qualitatively equivalent to the presented above, which could be validated using codes that simulate the seismoelectric response of layered 3-D media to point seismic sources like the ones given in Garambois & Dietrich (2002), Warden *et al.* (2013) and Zheng *et al.* (2021).

Despite of the simplifying assumptions, the proposed phenomenological model provides important information about the generation mechanism of IR and evanescent waves, suggesting that both conversions are physically equivalent. This is to say, both are generated by the same charge-separation mechanism, being the main difference that the IR is produced only by the dipoles located near the zero-offset (Garambois & Dietrich 2002) and the evanescent waves by the dipoles located at higher offsets, resulting in the observed relative amplitudes. Concerning the evanescent waves, we highlight the fact that the linear superposition of EM field generated

Downloaded from https://academic.oup.com/gji/article/236/1/62/7328943 by guest on 22 January 2024

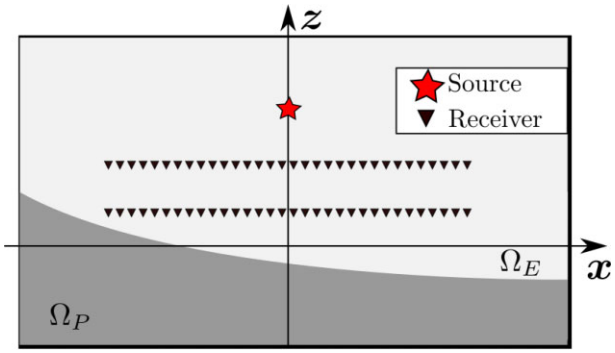

Figure 15. Representation of model C, composed by an elastic layer Ω_E over a poroelastic half-space Ω_P. The interface has a convex geometry and a depth of $z = -30$ m for zero offset. The source and receiver locations are the same of those considered in model B.

by the electric dipoles results in a signal with a seismic-like propagation velocity, as is the case of the coseismic signals in poroelastic media. Although at the considered frequencies, the inductive contribution is rather small, the fact that it is not taken into account in the SPM could play a part in the differences observed between its results and those of the PSVTM. This is to say, the SPM only takes into account the electric fields generated by the charge-accumulation mechanism, ignoring the electric fields that may be generated by magnetic field temporal variations, which are present in the seismoelectric phenomenon (Haines & Pride 2006), and are taken into account in the PSVTM code.

Another interesting matter is the choice of the derivative of the seismic source as the time signature of the dipole fields. Our tests indicate that this choice captures the relative amplitudes and waveforms of the seismoelectric conversions more accurately than other time signatures such as that of the wave front itself. In the PSVTM code simulations of the elastic/poroelastic model, we observed that the fluid relative-to-solid displacement field below the interface has a time signature similar to the electric field over the interface. We assume, therefore, that the charge accumulation giving rise to the latter follows the same temporal behaviour and direction as the former. Both times signatures are similar to the time derivative of the wavelet source (i.e. the derivative of the Ricker wavelet in our tests). This can be seen in Fig. 18, where we show both the vertical component of the electric field recorded at $z = 100$ m (over the interface between the elastic and poroelastic media) and the vertical fluid relative to solid displacement at $z = -10$ m (below the interface), and the wavelet source derivative. Additionally, although for the sake of conciseness we do not show it here, we observe in our PSVTM code tests that the solid particle velocity exhibits this same temporal signature, which is consistent with Grobbe *et al.* (2020).

Regarding the dipoles orientation, this direction approximates the one of the wave-induced pressure gradient, which in turn induces relative fluid motion below the interface. This was qualitatively described in Butler *et al.* (2018), where it is proposed that the *P* wave crossing the interface at oblique angles induces the charge-separation which generates the quasi-coseismic fields. As we observe, this is a good approximation, which avoids the introduction of poroelastic medium properties into the SPM. The dipoles reorientation improves the results of the SPM, especially for the case of non-horizontal interfaces, as model C.

We know that when dealing with perfectly elastic media, there is no reason to consider the modelling of EM fields due to the non-existence of electrokinetic coupling. However, this may still be valid when considering porous media with poor pore interconnection, that is, those with ineffective porosity or very low permeability. Wave propagation in these media can be modelled by replacing them with effective elastic ones. If we consider such media in contact with other ones that do present electrokinetic coupling, the SPM could be useful. An example would be a reservoir rock in contact with a seal layer with ineffective porosity (Zhang *et al.* 2019).

Finally, it is worth to stress that although the SPM relies on several simplifying assumptions, it is able to successfully explain the relative amplitudes of the numerically modelled seismoelectric responses in various hypothetical scenarios. As it was conceived, both IR and evanescent wave responses arise as a consequence of the same physical phenomenon. Their differences are merely owed to the geometrical disposition and activation time of the dipoles, which govern the way the superposition of their radiation patterns occurs. Maybe the first step towards an improvement of the present model could be to gain a better understanding of the seismic-to-EM energy conversion taking place at the interface. As mentioned before, this task can be addressed by computing the reflection and transmission coefficients, which in turn could provide expressions for the absolute amplitude of the radiation pattern of the dipoles. Another matter of forthcoming studies is to extend the proposed model to 3-D geometries and general irregular interfaces, which has several geophysical applications. This would also provide considerable advantages regarding computational costs.

5 CONCLUSIONS

In this work, we developed a phenomenological model to represent the 2-D seismoelectric response of an elastic medium over a saturated poroelastic medium. This model is constructed by a series of electric dipoles that are activated successively, simultaneously with the arrival of a seismic wave at the interface that separates the media. We tested the performance of the phenomenological model by comparing its results with those of a code that solves Pride's PSVTM equations for three models with different geometries. In these comparisons, we observe the ability of the SPM to represent both the IR and the evanescent wave generated at the elastic/poroelastic contact, that is, the complete seismoelectric response in the elastic medium. In addition, the amplitude ratio between the modelled seismoelectric conversions was also faithfully reproduced by the SPM. We highlight the independence of the SPM on the physical properties of the lower poroelastic medium. Instead, the SPM only depends on the parameters that compose the seismic source and the elastic medium. In particular, we show that the evanescent wave decays in amplitude with increasing source central frequency (and vice versa), due to the destructive interference phenomenon. In summary, the amplitude ratio between the seismoelectric conversions of a medium that does not have electrokinetic coupling (as in the elastic case) in contact with another medium that does (as in the poroelastic case), mainly depends on the seismic velocity of the first medium, the geometry of both the wave front and the interface, and the time signature of the mechanical source. Additionally, the SPM demonstrates that the superposition of EM fields propagating at EM velocities can result in signals with much lower velocities, such as seismic signals.

From the analysis of these comparisons, we can conclude that the SPM is a significant tool for understanding the generation mechanism of seismoelectric conversions. On the other hand, it also provides a fast way to compute this response, allowing to study its

Downloaded from https://academic.oup.com/gji/article/236/1/62/7328943 by guest on 22 January 2024

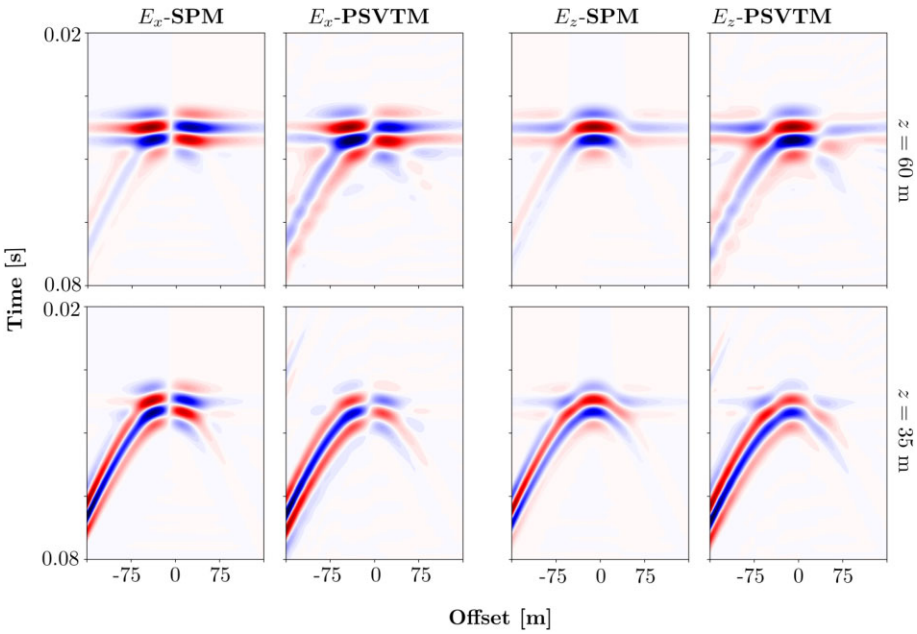

Figure 16. Results for model C: comparison between the SPM gathers (first and third columns) and the PSVTM gathers (second and fourth columns) for E_x (left-hand panels) and E_z (right-hand panels), for different receivers line distance to the interface: $z = 25$ m (upper panels) and 5 m (bottom panels). The central frequency of the source is 120 Hz. Again, the gathers show the two signals corresponding to the IR and the evanescent wave, both being stronger for negative offsets than for positive offsets. With decreasing receivers line distance to the interface, both the SPM and the PSVTM gathers show the amplitude of the IR increasing relative to the evanescent wave amplitude.

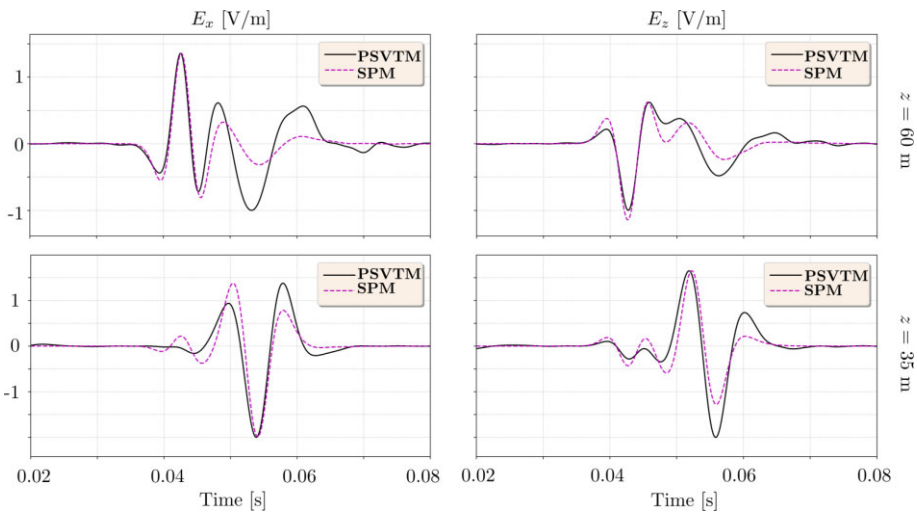

Figure 17. Results for model C: comparison between individual traces for E_z of the PSVTM (solid curves) and the SPM (dotted curves) at a source central frequency of 120 Hz. The receiver distance to the interface is 25 m (upper panel) and 5 m (bottom panel) and the offset is -90 m in both cases.

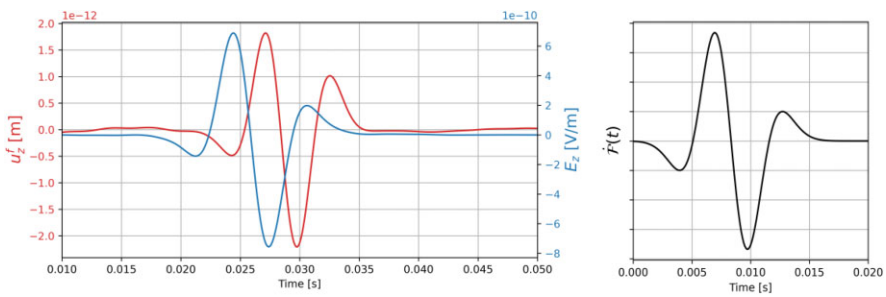

Figure 18. Left: individual traces of the vertical fluid relative to solid displacement (red curve) recorded in the poroelastic medium at 10 m of the interface, and the vertical electric field (blue curve) recorded in the elastic medium at $z = 100$ m. We observe that both time signatures are similar. Right: wavelet source derivative.

Downloaded from https://academic.oup.com/gji/article/236/1/62/7328943 by guest on 22 January 2024

behaviour with the different properties of the physical scenario under study. Finally, this characteristic is also very useful when designing efficient acquisition geometries for the study of the subsurface. In summary, we prove in this paper that the main characteristics of the seismoelectric conversions at an elastic/poroelastic interface can be fairly well modelled by means of a simple phenomenological approach with a minimum computational cost.

ACKNOWLEDGMENTS

The authors acknowledge support from FonCyT through grant PICT 2019-03220 and from CONICET through grant PIP 11220200101056CO. This work used computational resources from CCAD—Universidad Nacional de Córdoba (https://ccad.unc.edu.ar/), which is part of SNCAD MinCyT, República Argentina.

DATA AVAILABILITY

The codes used in this manuscript are available upon request to the corresponding author.

REFERENCES

Backus, G. & Mulcahy, M., 1976. Moment tensors and other phenomenological descriptions of seismic sources - ii discontinuos displacements, *Geophys. J. R. astr. Soc.,* **47,** 301–329.

Bordes, C., Sénéchal, P., Barrière, J., Brito, D., Normandin, E. & Jougnot, D., 2015. Impact of water saturation on seismoelectric transfer functions: a laboratory study of coseismic phenomenon, *Geophys. J. Int.,* **200,** 1317–1335.

Burgers, J.M., 1935. *Mechanical Considerations Model Systems-phenomenological Theories of Relaxation and of Viscosity,* Vol. **1,** Nordemann Publishing Company.

Butler, K., 1996. *Seismoelectrics effects of electrokinetic origin,* PhD thesis, University of British Columbia, Vancouver, Canada.

Butler, K.E., Kulessa, B. & Pugin, A.J., 2018. Multimode seismoelectric phenomena generated using explosive and vibroseis sources, *Geophys. J. Int.,* **213**(2), 836–850.

Chisari, C., Rizzano, G., Amadio, C. & Galdi, V., 2018. Sensitivity analysis and calibration of phenomenological models for seismic analyses, *Soil Dyn. Earthq. Eng.,* **109,** 10–22.

Corredor, R.M., Santos, J., Gauzellino, P. & Carcione, J., 2014. Reflection and transmission coefficients of a single layer in poroelastic media, *J. acoust. Soc. Am.,* **135**(16), 3151–3162.

Dupuis, J.C., Butler, K.E. & Kepic, A.W., 2007. Seismoelectric imaging of the vadose zone of a sand aquifer, *Geophysics,* **72,** A81–A85.

Dzieran, L., Thorwart, M., Rabbel, W. & Ritter, O., 2019. Quantifying interface responses with seismoelectric spectral ratios, *Geophys. J. Int.,* **217**(1), 108–121.

Dzieran, L., Thorwart, M. & Rabbel, W., 2020. Seismoelectric monitoring of aquifers using local seismicity-a feasibility study, *Geophys. J. Int.,* **222**(2), 874–892.

Gao, Y., Huang, F. & Hu, H., 2017a. Comparison of full and quasi-static seismoelectric analytically-based modeling, *J. geophys. Res.: Solid Earth* , doi:10.1002/2017JB014251.

Gao, Y., Wang, M., Hu, H. & Chen, X., 2017b. Seismoelectric responses to an explosive source in a fluid above a fluid-saturated porous medium, *J. geophys. Res.: Solid Earth,* **122**(9), 7190–7218.

Gao, Y., Wang, D., Yao, C., Guan, W., Hu, H., Zhang, W., Tong, P. & Yang, Q., 2019. Simulation of seismoelectric waves using finite-difference frequency-domain method: 2D SHTE mode, *Geophys. J. Int.,* **216**(1), 414–438.

Garambois, S. & Dietrich, M., 2002. Full waveform numerical simulations of seismoelectromagnetic wave conversions in fluid-saturated stratified porous media, *J. geophys. Res.,* **107**(B7), ESE5–1, doi:10.1029/2001JB000316.

Grobbe, N., Revil, A., Zhu, Z. & Slob, E., 2020. *Seismoelectric Exploration: Theory, Experiments, and Applications, Geophysical Monograph Series,* Wiley.

Guan, W., Hu, H. & Wang, Z., 2013. Permeability inversion from low-frequency seismoelectric logs in fluid-saturated porous formations, *Geophys. Prospect.,* **61,** 120–133.

Guan, W., Shi, P. & Hu, H., 2017. Contributions of poroelastic-wave potentials to seismo- electromagnetic wavefields and validity of the quasi-static calculation: a view from a borehole model, *Geophys. J. Int.,* doi:10.1093/gji/ggx417.

Haartsen, M.W. & Pride, S., 1997. Electroseismic waves from point sources in layered media, *J. geophys. Res.,* **102,** 24745–24769.

Haines, S.H. & Pride, S.R., 2006. Seismoelectric numerical modeling on a grid., *Geophysics,* **71**(6), 57–65.

Hilterman, F., 1975. Amplitude of seismic waves; a quick look, *Geophysics,* **40**(5), 745–762.

Hu, H. & Liu, J., 2002. Simulation of the converted electric field during acoustoelectric logging, in *72nd SEG Annual International Meeting, Expanded Abstracts,* Vol. **21,** pp. 348–351. https://doi.org/10.1190/1.1817249.

Hu, H. & Wang, K., 2000. Simulation of an acoustically induced electromagnetic field in a borehole embedded in a porous formation, in *Borehole Acoustics and Logging Reservoir Delineation consortis, Annual Report, Earth Resources Laboratory Industry Consortia Annual Report 2000-13,* eds Hu, H., Wang, K. & Wang, J.pp. 13–1-13-20, MIT. https://dspace.mit.edu/handle/1721.1/75724.

Hu, H., Guan, W. & Harris, J., 2007. Theoretical simulation of electroacoustic borehole logging in a fluid-saturated porous formation, *J. acoust. Soc. Am.,* **122,** 135–145.

Kulessa, B., Murray, T. & Rippin, D., 2006. Active seismoelectric exploration of glaciers, *Geophys. Res. Lett.,* **33,** L07503, doi:10.1029/2006GL025758.

Liu, Z., Yuan, L., Zhang, X., Liu, Z. & Wu, H., 2008. A laboratory seismoelectric measurement for the permafrost model with a frozen-unfrozen interface, *Geophys. Res. Lett.,* **35,** L21404 , doi:10.1029/2008GL035724.

Macchioli-Grande, F., Zyserman, F., Monachesi, L., Jouniaux, L. & Rosas-Carbajal, M., 2020. Bayesian inversion of joint SH seismic and seismoelectric data to infer glacier system properties, *Geophys. Prospect.,* **68**(5), 1633–1656.

Mavko, G., Mukerji, T. & Dvorkin, J., 2009. *The Rock Physics Handbook: Tools for Seismic Analysis of Porous Media,* Cambridge University Press.

Monachesi, L., Zyserman, F. & Jouniaux, L., 2018a. An analytical solution to assess the SH seismoelectric response of the vadose zone, *Geophys. J. Int.,* **213,** 1999–2019.

Monachesi, L., Zyserman, F. & Jouniaux, L., 2018b. SH seismoelectric response of a glacier: an analytic study, *J. geophys. Res.: Earth Surface,* **123**(9), 2135–2156.

Munch, F. & Zyserman, F., 2016. Detection of non-aqueous phase liquids contamination by SH-TE seismoelectrics: a computational feasibility study, *J. appl. Geophys.* , doi:10.1016/j.jappgeo.2016.03.026.

Pride, S., 1994. Governing equations for the coupled electromagnetics and acoustics of porous media, *Phys. Rev. B,* **50,** 15678–15695.

Pride, S. & Haartsen, M.W., 1996. Electroseismic wave properties, *J. acoust. Soc. Am.,* **100,** 1301–1315.

Rasolofosaon, P., 2009. Unified phenomenological model for the mechanical behavior of rocks, *Geophysics,* **74**(5), 107–116.

Ren, H., Huang, Q. & Chen, X., 2016a. Existence of evancescent electromagnetic waves resulting from seismoelectric conversion at a solid-porous interface, *Geophys. J. Int.,* **204**(1), 147–166.

Ren, H., Huang, Q. & Chen, X., 2016b. Numerical simulations of seismoelectromagnetic fields associated with a fault in a porous media, *Geophys. J. Int.,* **206**(1), 205–220.

Ren, H., Huang, Q. & Chen, X., 2018. Quantitative understanding on the amplitude decay characteristic of the evanescent electromagnetic waves generated by seismoelectric conversion, *Pure appl. Geophys.,* **175**(8), 2853–2879.

Rosas-Carbajal, M., Jougnot, D., Rubino, J., Monachesi, L., Linde, N. & Holliger, K., 2020. Seismoelectric Signals Producedc by Mesoscopic

Downloaded from https://academic.oup.com/gji/article/236/1/62/7328943 by guest on 22 January 2024

Heterogeneities, in *Seismoelectric Exploration: Theory, Experiments, and Applications,* chap. 19, pp. 249–287, eds Grobbe, N., Revil, A., Zhu, Z. & Slob, E., Wiley.

Smeulders, D. M.J., Grobbe, N., Heller, H. K.J. & Schakel, M., 2014. Seismoelectric conversion for the detection of porous medium interfaces between wetting and nonwetting fluids, *Vadose Zone J.,* doi:10.2136/vzj2013.06.0106.

Thompson, A.H. & Gist, G.A., 1993. Geophysical applications of electrokinetic conversion, *Leading Edge,* **12,** 1169–1173.

Thompson, A.H., Monachesi, L.B., Zyserman, F.I. & Jouniaux, L., 2023. Enhanced electroseismic coupling at charged interfaces, *Geophysics,* doi:10.1190/geo2021-0761.1.

Wang, D., Gao, Y., Yao, C., Wang, B. & Wang, M., 2020. Seismoelectric and electroseismic responses to a point source in a marine stratified model, *Geophys. Prospect.,* **68**(6), 1958–1979.

Wang, Y., Takenaka, H. & Furumura, T., 2000. Modelling seismic wave propagation in a two-dimensional whole-earth model using the pseudospectral method., *Geophys. J. Int.,* **145,** 689–708.

Warden, S., Garambois, S., Sailhac, P., Jouniaux, L. & Bano, M., 2012. Curvelet-based seismoelectric data processing, *Geophys. J. Int.,* **190,** 1533–1550.

Warden, S., Garambois, S., Jouniaux, L., Brito, D., Sailhac, P. & Bordes, C., 2013. Seismoelectric wave propagation numerical modeling in partially saturated materials, *Geophys. J. Int.,* **194,** 1498–1513.

Yan, F. & Vernik, L., 2021. Phenomenological models for estimating and constraining c13 for transversely isotropic hydrocarbon source rocks, *Geophysics,* **86**(5), 255–260.

Zhang, Y., Gao, J., Han, W. & He, Y., 2019. A discontinuous galerkin method for seismic wave propagation in coupled elastic and poroelastic media, *Geophys. Prospect.,* **67**(5), 1392–1403.

Zheng, X.-Z., Ren, H., Butler, K.E., Zhang, H., Sun, Y.-C., Zhang, W., Huang, Q. & Chen, X., 2021. Seismoelectric and electroseismic modeling in stratified porous media with a shallow or ground surface source, *J. geophys. Res.: Solid Earth,* **126**(9), e2021JB021950, doi:10.1029/2021JB021950.

Zyserman, F., Gauzellino, P. & Santos, J., 2010. Finite element modeling of SHTE and PSVTM electroseismics, *J. appl. Geophys.,* **72,** 79–91.

Zyserman, F., Gauzellino, P. & Santos, J., 2012. Numerical evidence of gas hydrate detection by means of electroseismics, *J. appl. Geophys.,* **86,** 98–108.

Zyserman, F., Jouniaux, L., Warden, S. & Garambois, S., 2015. Borehole seismoelectric logging using a shear-wave source: possible application to CO_2 disposal?, *Int. J. Greenhouse Gas Contr.,* **33,** 82–102.

Zyserman, F., Monachesi, L. & Jouniaux, L., 2017. Dependence of shear wave seismoelectrics on soil textures: a numerical study in the vadose zone, *Geophys. J. Int.,* **208**(2), 918–935.

Zyserman, F., Gauzellino, P. & Jouniaux, L., 2020. Finite element modeling of electroseismics and seismoelectrics, in *Seismoelectric Exploration: Theory, Experiments, and Applications,* chap. 18, pp. 245–267, eds Grobbe, N., Revil, A., Zhu, Z. & Slob, E., Wiley.

Zyserman, F.I., Monachesi, L.B., Thompson, A.H., D'Biassi, T., Jouniaux, L. & Gauzellino, P., 2022. Numerical modelling of passive electroseismic surveying, *Geophys. J. Int.,* **230**(3), 1467–1488.

Downloaded from https://academic.oup.com/gji/article/236/1/62/7328943 by guest on 22 January 2024

© The Author(s) 2023. Published by Oxford University Press on behalf of The Royal Astronomical Society. This is an Open Access article distributed under the terms of the Creative Commons Attribution License (https://creativecommons.org/licenses/by/4.0/), which permits unrestricted reuse, distribution, and reproduction in any medium, provided the original work is properly cited.